ARTICLE OPEN

Check for updates

Beryllene, the lightest Xene

Sumit Chahal [1], Arkamita Bandyopadhyay[2], Chan-Shan Yang [3,4 ✉] and Prashant Kumar[1,5 ✉]

After the discovery of sp²-hybridized graphene and even lighter borophene, the scientific quest for the thinnest metallic sheets prompts the discovery of beryllene. As beryllium lacks p-electrons, the hybridization and structural evolution of beryllene in determining electronic/excitonic behaviors are scientifically interesting. Herein, we report the experimental realization of freestanding flat beryllene sheets with a lateral dimension of ~0.2–4 μm via sonochemical exfoliation. High-resolution transmission electron microscopy establishes the existence of hexagonal, square and stripe crystallographic phases. While characteristic Raman fingerprints ~451 and ~614 cm^{-1}, and experimentally observed electrically metallic nature of beryllene (vindicated by density-functional-theory band structure calculations) establish beryllene synthesis. Room temperature magnetism in Be-G and Be-CNT hybrids (established by Raman mapping and magnetic force microscopic imaging) is an interesting finding. Beryllene was explored as a surface-enhanced Raman spectroscopy (SERS) anchor in molecular sensing, oxidation-resistant, and fire-resistant laminates. It is believed that the discovery of beryllene will lead to novel functionalities and emerging applications.
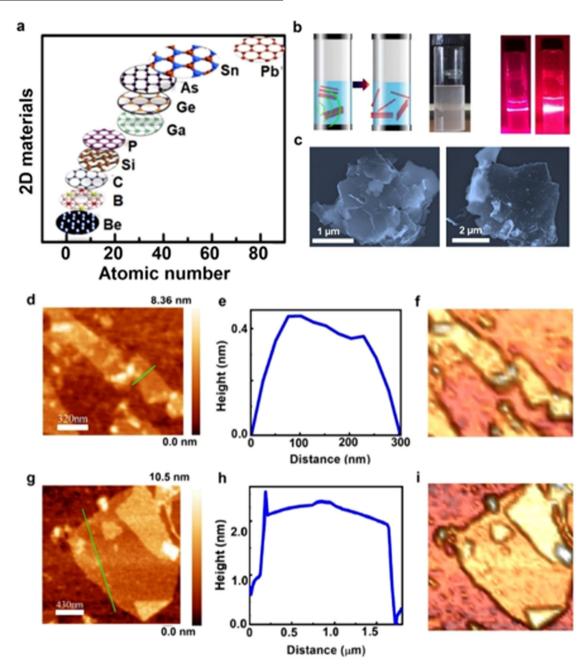
INTRODUCTION

In the family of Xenes, graphene was the first member to be exfoliated. Apart from its quantum excitonic behavior, it also has the record electronic mobility[1–3]. Phosphorene, silicene, germanene, stannene, arsenene, plumbene, and borophene were subsequently accomplished in experiments[4–16]. Very recently, two-dimensional (2D) gold was also attained[17]. Every other day a new Xene is discovered, and then its new applications are explored[18–24]. From the materials perspective, most of the Xenes exhibit Dirac or Dirac-like behaviors, which provide them a unique identity as quantum materials. Interestingly, these materials exhibit quantum behaviors[25]. The quantum Hall effect in graphene, strain-induced modulation of quantum states, super-conductivity in the twisted bilayer of graphene, and coupling states in hybrids of Xenes are some of the salient examples[1,26]. Lightweight, thermal stability against oxidation, thermal conductivity, and structural fidelity, apart from electronic nature, are crucial characteristics determining the potential of Xenes for a variety of frontline applications, including light combat aircrafts (LCA), missiles, satellites, thermal packaging, trace-level disease diagnosis via surface-enhanced Raman spectroscopy (SERS), oxidation-resistant laminates, laser shielding, and transparent conducting layers, optoelectronics and single photon emission[27–32]. Beryllium, an s-block element, has a high melting point of 1287 °C and is thermally stable up to 1000 °C against oxidation. The Young's modulus of beryllium is 287 GPa, which signifies high structural rigidity. Its specific heat is 1925 J Kg^{-1} K^{-1}; its coefficient of thermal expansion is 11.4×10^{-6} K^{-1}, which makes it stable under thermal and mechanical loading. Its thermal conductivity is 216 Wm^{-1}K^{-1}, which makes it suitable for thermal management[33]. The thermal stability against oxidation for the 2D phase of beryllium (henceforth called beryllene) is expected to be even better than phosphorene. A new generation of electronic, photonic, thermal, and thermoelectric devices is expected to emerge. Contrary to graphene and borophene, a beryllene sheet (comprising of atoms of s-block element beryllium) is expected to be severely electron-deficient, which restricts it from forming sp or sp² hybridization in its flat geometry in the ground state energy configurations. Therefore, even more interesting structural chemistry is expected, which would ultimately govern the existence of various structural phases of beryllene. In fact, beryllene is expected to exhibit remarkable physical and chemical behavior due to the possibility of unusual binding, such as three-center two-electron binding[34] in order to share a limited number of available electrons, which will lead to a new territory of device functionalities and sensing capabilities. All the attributes of beryllium mentioned above make it very exclusive, rendering it worth exploring its 2D phase.

Extreme urgency and natural curiosity combined led us to the discovery of beryllene, and in this article, we report our salient findings. Beryllene was synthesized by liquid-phase sonochemical exfoliation of microcrystalline beryllium powder in dimethylformamide (DMF) solvent followed by separation employing centrifugation. A host of microscopic (field emission scanning electron, atomic force, transmission electron) and spectroscopic (UV-Vis, Raman, and X-ray photoelectron (XPS)) techniques have been employed to characterize synthesized beryllene sheets. Two-probe resistivity measurements were carried out to evaluate electronic character. SERS-based molecular sensing of methylene blue has been demonstrated by beryllene-based plasmonic platforms. Hybrids of beryllene with CNTs and graphene have been synthesized, and their magnetic nature is explored[35–37].

RESULTS AND DISCUSSION
Discovery of beryllene

The atomic number of beryllium is 4, and therefore, if its 2D phase can experimentally be realized, it will be the lightest known 2D material (see Fig. 1a). In order to obtain 2D sheets of beryllene, we employed a sonochemical synthesis procedure (illustrated in
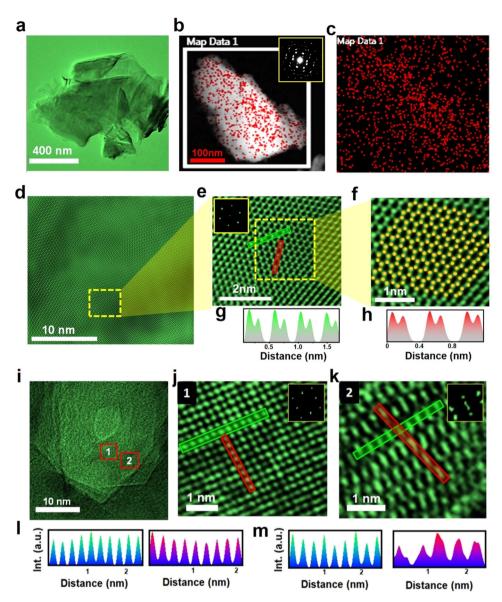
[1]Department of Physics, Indian Institute of Technology Patna, Bihta Campus Patna-801106, India. [2]The Bremen Center for Computational Materials Science (BCCMS), Universität Bremen, Am Fallturm 1, TAB Building, 28359 Bremen, Germany. [3]Institute and Undergraduate Program of Electro-Optical Engineering, National Taiwan Normal University, Taipei 11677, Taiwan. [4]Micro/Nano Device Inspection and Research Center, National Taiwan Normal University, Taipei 106, Taiwan. [5]Global Innovative Centre for Advanced Nanomaterials (GICAN), University of Newcastle, NSW-2308 Newcastle, Australia. ✉email: csyang@ntnu.edu.tw; Prashant.Kumar@newcastle.edu.au

Fig. 1 **Sonochemical synthesis of beryllene. a** Schematic diagram representing various Xenes discovered so far according to their atomic number. **b** Schematic layout of sonochemical exfoliation of beryllene along with Tyndall effect for beryllene sheets centrifuged at 6k and 3k RPM in dimethylformamide (DMF). **c** FESEM image of an exfoliated sheet of beryllene having lateral dimension ~3 μm. **d–f** AFM image of exfoliated beryllene sheets and line profile depicting monolayer along with the 3D view of sheets. **g–i** AFM image of multilayer beryllene along with its line profile depicting sheets height ~2 nm and its 3D view.

Fig. 1b). A semi-transparent grayish solution is formed upon sonication in the DMF solvent for 20 h. Filtering by centrifugation of the supernatant was used for microscopy. While the laser beam dispersion observed in the Tyndall effect for the supernatant of beryllene in DMF medium is significantly vivid for 3000 RPM (revolutions per minute), it is almost absent at 6000 RPM. (see Fig. 1b and more details in Supplementary Figs. 1 and 2). To our surprise, we indeed obtained a sheet-like structure in the field-effect scanning electron microscope (FESEM) with lateral dimensions ~3 μm (see Fig. 1c), where layered features are present on the top surface. Atomic force microscope (AFM) imaging provided further proof that a monolayer of beryllene has indeed formed (See Fig. 1d, f for 2D and 3D view), which is evident from the line

profile in Fig. 1e. The AFM image of multilayer beryllene along with its line profile and 3D view were shown in Fig. 1g–i. The sonochemical process involves solvent (DMF in the present case) to chip-in between the layers from the edge, and upon the ultrasound treatment, cavitation takes place, weakening interlayer coupling and giving rise to exfoliation. Apart from the exfoliation, ultrasound energy fragments the sheet as well, and this is the reason that monolayer or a few monolayer sheets have nano to micrometer lateral dimensions (see Supplementary Fig. 3). Even though the lateral dimension of the sheet is small at the micron scale for a few (1–3) layers, such dimensions are sufficient for nanoscale device fabrication and demonstrations of electronic chips and sensors. Beryllene material itself has never been
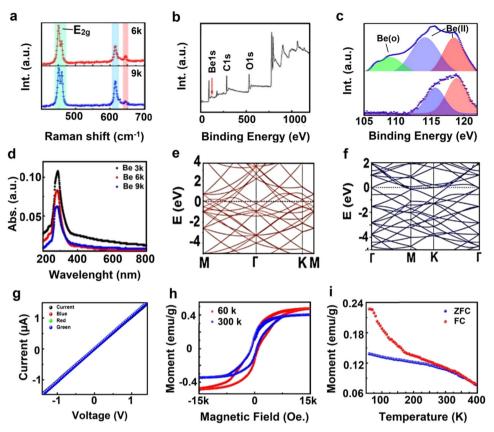
Fig. 2 Transmission electron microscopy. a TEM image of transparent beryllene sheets of micrometer dimensions. **b, c** The elemental mapping of beryllene confirms the presence of constituent element Be, inset having selected area electron diffraction (SAED) exhibits various symmetries (twofold, fourfold and sixfold). **d** Large-area HRTEM image of beryllene. **e** Zoomed-in image of marked region in (**d**) showing the hexagonal atomic arrangement of atoms. **f** False color atoms indexed over the beryllene atoms to visualize hexagonal configuration. **g, h** Atomic line profile of (**e**) along two directions marked by green and red lines has an interatomic distance of 1.6 Å and 1.3 Å, respectively. **i** HRTEM atomic image of exfoliated beryllene, **j, k** HRTEM atomic image of a square phase of beryllene and striped phase of beryllene. **l** Atomic line profiles of (**j**) having interatomic separation 2.4 Å (green line) and 2.4 Å (red line). **m** Atomic line profile of the striped phase shown in (**k**) having interatomic separation is 2.8 Å (green line) and 1.81 Å (red line).

experimentally realized before, which makes it exceptionally special.

Atomic structure determination

A natural curiosity is how beryllium atoms with electronic configuration $1s^2 2s^2$ can form a sheet, and this is exactly why it has not been explored experimentally. In contrast to graphene, which is made up of carbon atoms having electronic configuration $1s^2 2s^2 2p^2$ and whose 2D lattice has sp^2-hybridized atoms, borophene composed of boron atoms with electronic configuration $1s^2 2s^2 2p^1$ is comparatively electron-deficient and exhibits exclusive three-center two-electron[30] binding to fulfill valances. Interestingly, while graphene is semi-metallic, borophene exhibits metallic behavior. However, the beryllene sheet, which is made up of beryllium atoms with electronic configuration $1s^2 2s^2$, does not

have a 2p orbital and is certainly poorer than borophene in the number of electrons. Thus, beryllene seems an extremely promising 2D material. During the natural processing of extraction and crystal formation itself, if several atoms are brought together and energetically excited up to the level where 2s electrons can jump to 2p orbital, then there is a possibility of sp and even sp^2 hybridization to occur. This exotic bond formation would enrich the unique surface interaction and catalytic functionality of the material. We observed transparent beryllene sheets having folds at the edges in TEM imaging, which are characteristics of mono or few layer atomic sheets (see Fig. 2a). Elemental mapping has been performed to confirm the presence of constituent element beryllium (see Fig. 2b, c). Large-area HRTEM image of beryllene has different atomic configurations (see Fig. 2d). The zoomed-in Fig. 2e clearly displays the hexagonal atomic configuration of

Fig. 3 Spectroscopic characterizations and magnetic behavior of beryllene. a Raman fingerprints of beryllene sheets centrifuged at 6k RPM and 9k RPM at 451, 614, and 645 cm^{-1}. **b** XPS survey spectra C 1s of beryllene. **c** XPS plots of B 1s of beryllene (bottom-plot), beryllene after 2-h argon plasma itching (top-plot). **d** UV-Visible absorption spectra of beryllene supernatant centrifuged at 3k, 6k, and 9k RPM. **e** Calculated band structure diagram of beryllene exhibiting metallic behavior. **f** Calculated band structure diagram of bilayer beryllene. **g** I-V/PC behavior of beryllene with optical excitation by red, green, and blue lasers. **h** Magnetization vs magnetic field (M-H) hysteresis curve of beryllene measured at room temperature (300 K) and at low temperature (60 K). **i** Magnetization vs temperature (M-T) plot of beryllene having Field cooled (FC) and zero field cooled (ZFC) behavior of beryllene, the field used for Field-cooled measurements was 1000 Oe.

beryllium atoms along with fast Fourier transform (FFT) patterns having bright dots, suggesting a hexagonal lattice symmetry. For more visual clarity, we index the zoomed-in HRTEM image by false color atoms over beryllene atoms (see Fig. 2f). The smallest interatomic distances corresponding to beryllene along two symmetry directions are 0.16 nm (green line) and 0.13 nm (red line) normal to it (see Fig. 2g, h respectively). We obtain a beryllene hexagonal atomic configuration with an interatomic distance of 1.3 Å in contrast to 1.42 Å of graphene and 1.50 Å in borophene. Graphene has a single crystallographic phase, while the electron-deficient character of borophene drives to a large number of atomic configurations starting from two-center two-electron bonds up to seven-center two-electron bonds[38]. Multi-center polymorphic configurations lead up to 16 bulk allotropes of boron, a variety of lattice configurations that lie within a narrow range of energies set apart by hexagonal holes, making 2D boron adopt a structure depending on the substrate compared to other 2D materials. Similarly, beryllene lacks electrons; therefore, it may form a varying number of crystallographic phases. Even the 3D form of beryllium is not thermodynamically stable, and therein difference in different structure evolves. We were really surprised to observe that crystalline beryllene sheets were hexagonal in shape and were displaced and twisted at an angle, which is characteristic of 2D materials (see Fig. 2i). Incidentally, we could observe two distinct crystallographic phases of beryllene. The first phase has a square lattice (henceforth we call it square phase) with a ~ 2.4 Å and b ~ 2.5 Å (see Fig. 2j and line profiles in Fig. 2l). Interestingly, lattice parameters are different from those of BeO[39].

The second phase has two pairs of adjacent atoms in hexagons lifted up (henceforth, we call it the striped phase) and the remaining two atoms lying down, which are placed opposite to each other (see Fig. 2k and line profiles in Fig. 2m). The interatomic distance across the stripes (2.8 Å) and normal to it (1.8 Å) in Fig. 2k closely matches with Be thin films reported earlier[39]. Available ordering in these atomic structures can be analyzed through Fast Fourier Transform (FFT) as well. Lattice parameters in both the observed phases are very unique and match well with the lattice in crystalline Be film (within expected experimental limits) and, importantly, do not match with oxide. These observations are characteristic of beryllene atomic sheets.

Chemical phase investigation

Raman spectra display Raman active modes at 451 (E_{2g}) and 614 cm^{-1} (see Fig. 3a) were observed for the beryllene sheet obtained at centrifugation speed of 6k RPM and 9k RPM; these peaks match closely with the existing literature[39–41]. The Raman peak at 614 cm^{-1} arises due to quantum confinement, which is not found in thin films. Due to the structural instability (polymorphism) in beryllene crystal structure, close-by Raman peaks are expected; in fact, we have observed a split E^{2g} peak. The shoulder-like feature on the right side of the 451 cm^{-1} peak, in most probability, arises due to structural defects, and a tiny peak at 645 cm^{-1} arises due to the presence of surface-bound oxide. Moreover, the most stable crystalline beryllium oxide (BeO) phase exhibits a strong Raman peak at ~680 nm, which is absent in our Raman spectrum[40]. Interestingly, the surface-bound oxide-
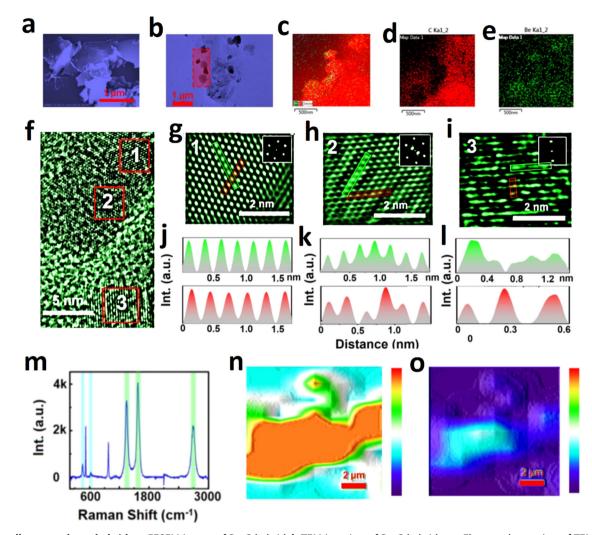
originated peak at 645 cm^{-1} is negligibly small with respect to those for the metallic peaks. When the centrifugation speed was raised to 9k RPM, resulting in thinner sheets that had nascent surfaces even they exhibited an ignorable oxide peak. However, thinner sheets exhibit a bit of an enhanced defect peak. This is expected as well, as a large number of layers provide better interlayer coupling resulting in the structural stability of the system, which is missing in the case of monolayers. It is expected that while monolayers and bilayers will predominantly exhibit the structurally vulnerable striped phase, multilayered sheets will exhibit the structurally stable square phase. Beryllium atomic size is small, and a p-orbital is not present in contrast to higher atomic number atoms such as carbon. This results in compromised X-ray absorption by beryllium atoms. Thus, in contrast to graphene and other heavier Xenes, the perception is that beryllene will exhibit a negligible XPS peak. We, however, could attain Be peak in XPS measurements (see Fig. 3b). Moreover, due to high reactivity, beryllium carries surface oxidation which is very significant in XPS measurements. Even the parent bulk beryllene powder predominantly exhibits surface oxidation. In order to detection of the Be in XPS, it is required the surface to be cleaned using argon etching. Upon exfoliation, one major peak was obtained in XPS, which was deconvoluted into two peaks around ~115 and 119 eV, which hints at the surface oxidation of beryllene (see Fig. 3c bottom plot). However, the metallic peak at ~108 starts evolving and upon plasma etching (Ar+ sputtering) of the surface, which is the signature of metallic beryllene (see Fig. 3c, upper plot)[42,43]. Moreover, the beryllium oxide exhibits a major peak at 94 eV and two satellite peaks around 87 and 77 eV; such peaks are not observed in obtained Be XPS spectrum[43]. The XRD of bulk beryllium consists of peaks at 45.6 (100), 50 (002), 51.9 (101), and 71.7 (102) (see Supplementary Fig. 4)[44]. The ultra-thin nature of 2D layers presents a challenge to the use of X-ray diffraction (XRD) analysis because of its low density and atomic mass; beryllium is relatively transparent to X-rays. The XRD of beryllene is obtained from the stacked 2D layers or for a few layers. Therefore, beryllene has a single peak at 49.4 (002), which corresponds to the hexagonal closed-packed crystalline system. The downshift in XRD of beryllene has been witnessed due to an increase in interlayer separation from bulk to a few layers.

Optical, electronic and excitonic behavior

As true with other existing Xenes, beryllene is expected to exhibit interesting physical properties such as optical, electrical, and excitonic behavior. We observed that while visible range absorption is 2–3% for samples filtered at 3k RPM centrifugation speed, it further reduces to abysmally small, below 1% for 6 and 9k RPM samples (see Fig. 3d). This is an expected result as metallic monolayers of beryllene will be highly optically transparent.

Beryllene, being a 2D material, triggered several natural curiosities. The very first issue concerns its binding. Sheet formation seems mysterious from a classical valance satisfaction point of view. However, under an excited state, it is quite feasible to have s-p hybridization as s-orbital electrons will populate p-orbital as well. The hexagonal 2D skeleton of Be atoms derived from its bulk structure[45] (metallic) was found to be a bound system (negative potential energy), hinting that 2D Be is possible (see the lattice considered for band structure calculation in Supplementary Fig. 5a). We have considered a hexagonal unit cell of Be (9 atoms) following the p63/mmc space group of its bulk form and found that the unit cell lengths are a = 6.33 Angstrom and b = 6.38 Angstrom. It does not follow a simple graphene-like two-atom unit cell structure because of the smaller size and electron count of the Be atoms. We have found that the system is metallic by calculating the band structure. MD calculation of Be layer is performed. It is performed at 300 K (room temperature simulation) for 50 ps. It shows ripples but does not show bond

breaking, indicating the stability of the system. The hexagonal phase exhibits a metallic band structure with a sort of parabolic band dispersion in the conduction band and close-to-linear band dispersion in the valence band(see Fig. 3e). When the strict hexagonal skeleton was relaxed in molecular dynamics for 50 ps, bond angles between the adjacent bonds flex a bit, and thus the material sheet assumes a new structure. In general, arrays of atoms lie a little above or below (see Supplementary Fig. 5b). Incidentally, bond angle flexing results in a phase close to the striped phase experimentally observed by us in HRTEM. It is interesting that even after 50 ps, the 2D phase is maintained, and the structure does not collapse (the bond does not break). Keeping in mind the time scale of molecular phenomena (fs-ps), 50 ps is a large time span, and it is a great observation that this 2D material exhibits structural strength. 3D protrusion arrays in beryllene occur at the atomic scale and seem to be an electron-sharing mechanism. Several other 2D materials, including 2D gallium nitride (GaN), exhibit structural irregularities at monolayer thickness, and they attain stability at higher layer thickness. The bilayer (top view in Supplementary Fig. 5c) calculation reveals that the two layers combine together to form a non-van der Wall sheet-like structure, where the charge density (see the charge density profile in Supplementary Fig. 5d) contribution comes mainly from the middle layer Be atoms. Incidentally, the bilayer exhibits a distinct DFT band structure (see Fig. 3f). When we go from monolayer to bilayer, symmetry seems to be changed, as is apparent from DFT band structure calculations. Infect the k indexing itself has changed due to a change in symmetry. Graphene is a perfectly Dirac material that exhibits linear energy dispersion; borophene also exhibits Dirac-like behavior having linear energy dispersion; however, its valence band is attached to adjacent atoms. DFT of beryllene exhibits non-linear dispersion at Γ point. The valence band and conduction band (both exhibiting parabolic energy dispersion) met at a point, and there is no energy band gap. The electronic/excitonic character of beryllene seems to be intriguing due to its interesting band structure. Four-probe electrical measurements on beryllene sheets exhibit metallic behavior (see Fig. 3g). Moreover, photothermal effects induced by focal laser heating in photoconductivity measurements have no impact on current.

Electron-deficient character makes beryllium a reactive metal. It is obviously challenging to achieve oxygen-free beryllene sheets. In order to get that, therefore, we have used dimethylformamide, which is a reducing solvent, to achieve beryllene with minimal oxygen content. Drying was done in a nitrogen environment to ensure the surface gets minimal oxygen adsorption. Beryllium is a light element, and its inherent electronic character to form several covalent bonds render it capable of forming several crystallographic structural phases. Two prominent phases (α and β) of beryllene have been predicted. While the α phase has a squarish atomic lattice, the β phase has a hexagonal atomic lattice with some atoms slightly off-plane (Figure below). Moreover, while the α phase was demonstrated to have semi-metallic yet Dirac-like behavior (close to graphene's linear energy dispersion at K-point), β phase, however, seems to have parabolic energy dispersion with conduction band minima slightly off-axis from valance band maxima. The values of cohesive energies of α- and β-beryllene calculated by them were found to be 2.93 and 3.29 eV, respectively, which are comparable to those of germanene (3.26 eV) and bulk Be (3.32 eV, experimental value). Even though these two phases have been theoretically determined and their thermal stability and band structures have been predicted, several other crystallographic phases with evenly distributed atomistic vacancies, linear chains of vacancies/vacancy clusters, atomic protrusions, and ridgelines are possible to form, similar to borophene phases. Varieties of these phases arise due to the urge of the crystal to relax strain in the lattice. Borophene, for

Fig. 4   Beryllene-graphene hybrids. **a** FESEM image of Be-G hybrid. **b** TEM imaging of Be-G hybrid. **c–e** Elemental mapping of TEM image, Be and carbon atoms are identified via color coding (Green for Be and Red for carbon (graphene)). **f** HRTEM image of Be-G hybrid depicts the different arrangements of atoms marked in three regions. **g** HRTEM image of region 1 of (**f**) bestows the hexagonal symmetry of atoms surrounding an atom in the center along with the FFT pattern. **j** Average interatomic distance in two directions, as marked in (**g**), was 0.254 nm (green line) and 0.29 nm (red line). **h** HRTEM image of Location 2 marked in the image (**f**). **k** The average interatomic distances for region 2 as zoomed-in (**h**) are 0.255 nm (green line) and 0.243, 0.270 and 0.245 (red line). **i** HRTEM image of section 3 of (**f**). **l** The average atomic distances were 0.256 nm along with the array of atoms (green line) and 0.28 nm perpendicular to the array of atoms (red line) of image (**i**). **m** Raman spectra of Be-G hybrid exhibits peaks at 457, 620 cm^{-1} correspond to Be and 1347, 1577 and 2691 cm^{-1} belong to graphene. **n** Peak intensity map of beryllene peak (~450 cm^{-1}). **o** Peak intrinsity map of graphene G peak (~1580 cm^{-1}).

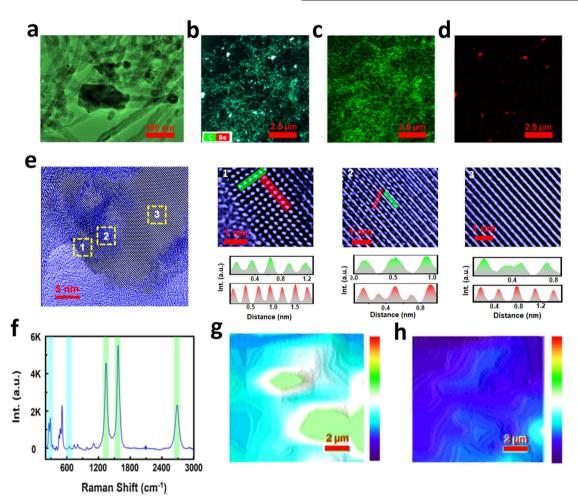example, has the capability to form unusual 2 electrons 3 center bonds; similarly, beryllene can have such bonds.

Magnetic behavior of beryllene

In order to investigate the magnetic behavior of beryllene, M-H hysteresis loop was obtained at 60 K and 300 K (see Fig. 3h). While the bulk beryllium is well known diamagnetic material (see Supplementary Fig. 6). Compared with the bulk, the hysteresis loop of beryllene exhibits higher saturation magnetization (Ms) 0.48 emu/g at 60 K with respect to that for 300 K (0.39 emu/g), which attributed to a 2D quantum confinement-induced enhancement of spin polarization with reduction of dimension[46]. The effect of temperature on the magnetic moment was also examined via magnetization vs temperature (M-T) measurement, as shown in Fig. 3i. Field-cooled (FC) and zero field-cooled (ZFC) curves depict splitting, indicating a rapid increase in the magnetic moment at low temperature with the applied field. An undoubted conclusion is that Curie point (~400 K) is beyond room temperature. Electron-deficient nature of the bond in beryllene will give

rise to uncompensated spin and will give rise to spin asymmetry. Spin asymmetry caused by structural instability (protrusion/ ridgelines) in beryllene crystal gives rise to ferromagnetism, as has been observed in our beryllene samples. At 180 K, though there is a mild transition evidenced in the FC curve, which signifies the onset of change in ordering. In general, Curie point above room temperature in a 2D sheet in mono-elemental material with significant Ms itself is very interesting. Graphene, for example, does not exhibit any significant magnetism in its pristine form. Also, magnetism arising in 2D graphene systems due to extrinsic reasons such as oxygen content, etc., almost vanishes at room temperature, and in this regard, beryllene fares better.

Magnetic behavior of berylline-based hybrids

2D-1D and 2D-2D hybrid nanosystems have been in the news recently due to novel quantum states they compose at the interface in ground or in excited states[47–53]. Keeping this in mind, we have explored Beryllene-CNT (Be-CNT) and Beryllene- graphene (Be-G) hybrids. Sonochemically synthesized beryllene
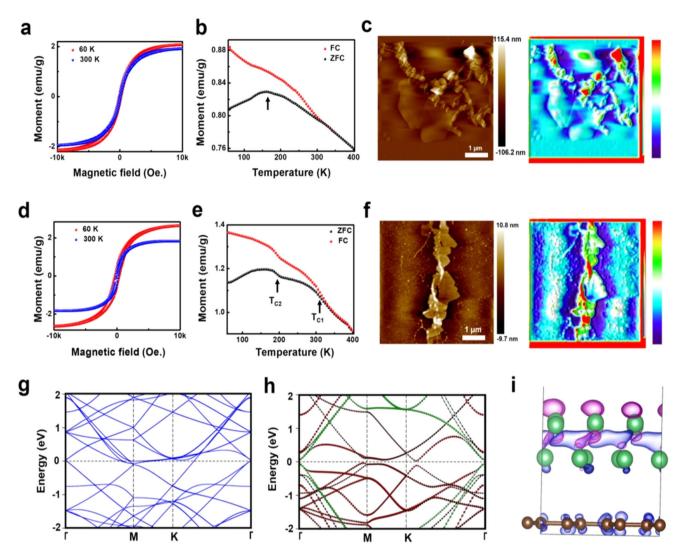
Fig. 5 Beryllene-CNT hybrids. a TEM image of Be-CNT hybrid. **b–d** TEM image along with the elemental mapping represented by green (C (CNT)) and red (Be)) colors. **e** HRTEM atomic image of Beryllene-CNT hybrid. HRTEM atomic images in zoomed-in areas (1–3). Atomic line profiles along two directions (bottom images in zoomed-in figures). **f** Raman fingerprints of Be-CNT hybrid having the signature of both be and CNT. **g** Peak intrensity map of carbon (G peak ~1580 cm^{-1}). **h** Peak intensity map of beryllene peak (~450 cm^{-1}).

supernatant was mixed with graphene or CNT supernatant and then microwave treated, which resulted in corresponding hybrids (see "Synthesis of hybrid" in "Methods" for details). Graphene or CNT being a good microwave absorber, gives a very high temperature at the interface within a few seconds upon microwave irradiation which results in exfoliation as well as hybridization of beryllene with graphene and CNT (see Supplementary Fig. 7). Various characterizations were performed for the synthesized hybrids. FESEM imaging (see Fig. 4a) exhibits sheets-like features for both Be and graphene; the color contrast depicts the difference in sheets—blackish sheets correspond to graphene and white belongs to Be. Electron imaging in TEM of Be-G hybrid is shown in Fig. 4b. The elemental mapping of Be-G hybrid shown by the color shading validates the presence of both materials (see Fig. 4c–e). Moreover, Beryllium, having low density and atomic number, becomes transparent to electron beams and X-rays as well. Besides, the regions of absence of carbon element in mapping represent presence of beryllene (see Fig. 4d). In order to dig into details, the HRTEM image is zoomed-in to see influences of hybridization on the arrangements of atoms in three different locations were analyzed (see Fig. 4f. The region 1 atomic arrangements depict the hexagonal symmetry of atoms surrounding an atom in the center corresponds to the beryllene (see Fig. 4g, inset FFT pattern showing one central dot surrounded by six dots). The average interatomic distances along two orientations of Fig. 4g are 0.254 nm (green line) and 0.29 nm (see Fig. 4j).

The region 2 has a different morphology of atoms which appear to be Moire patterns of hybridized Be and Graphene sheets (see Fig. 4h with inset FFT pattern showing two bright dots correspond to Be and graphene surrounding by hexagonal symmetry of dots hints for both materials). The average interatomic distances, in this case, is 0.255 nm (green) and 0.243, 0.270 and 0.245 (red, these values repeat and arise due to rippling, as evident in Fig. 4h), as shown in Fig. 4k. Region 3 has different atomic profiles, depicting a linear array of atoms (see Fig. 4i). The average atomic distances were 0.256 nm along with the array of atoms (green line) and 0.28 nm perpendicular to the array of atoms (red line) (see Fig. 4l). Chemical identification of Be-G hybrid employing Raman spectroscopy exhibits peaks at 457, 620 cm^{-1} correspond to Be and 1347, 1577 and 2691 cm^{-1} belong to graphene (see Fig. 4m). We identify a difference in hybridized 2D sheets of graphene and beryllene via Raman mapping. There is an overlap in peak intensity maps of Be and graphene, due to sheets of different materials the relative intensity provides a strong indication of layers of Be hybridized with graphene (see Fig. 4n, o). While peak intensity maps allow a step-by-step assignation of layer number, such mapping represents a clear and easy method of assigning the layers belonging to beryllene and graphene in Be-G hybrid[39–41,54,55].

TEM image of Be-CNT 1D-2D hybrid shown in Fig. 5a shows the CNT bundling and agglomeration. CNTs seem to have been hybridized with the partially transparent Be sheets. Electron
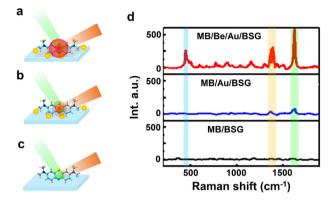
Fig. 6 Magnetic behavior of berylline-based hybrids. a Magnetization vs magnetic field (M-H) hysteresis curve of beryllene-graphene hybrid measured at low temperature (60 K) and at room temperature (300 K). **b** Magnetization vs temperature (M-T) plot of Be-G having Field cooled (FC) and Zero field cooled (ZFC) behavior, the field used for Field-cooled measurements was 1000 Oe. **c** MFM topography image of Be-G along with corresponding color intensity profile. **d** Magnetization vs magnetic field (M-H) hysteresis curve of beryllene-CNT hybrid measured at low temperature (60 K) and at room temperature (300 K). **e** Magnetization vs temperature (M-T) plot of Be-CNT having Field cooled (FC) and Zero field cooled (ZFC) behavior, the field used for Field-cooled measurements was 1000 Oe. **f** MFM topography image of Be-CNT along with corresponding color intensity profile. **g, h** DFT band structure diagram of Be and Be-G hybrid. **i** Charge density difference profile of Be-G hybrid.

imaging via TEM, along with the elemental mapping, is shown in Fig. 5b–d). It is also evident that the CNT tends to bulge out through the surface of Be sheets which appear scratchy and highly disordered. This depicts the formation of 2D Be-1D CNT hybrid morphology (see Fig. 5a, Supplementary Fig. 8). Fusions of CNTs with sheets at microwave focal points are apparent. The large-area HRTEM images reveal the presence of both beryllene and CNT lattice (see Fig. 5e, see more HRTEM images in Supplementary Fig. 8). The zoomed-in HRTEM images of marked region 1 in Fig. 5e display the square phase with interatomic distances along two directions ~2.7 Å (green line) and ~2.7 Å (red line) (see Fig. 5e and line profiles in Fig. 5h). The zoomed region 2 has hexagons arrangement of atoms (see Fig. 5e). The interatomic distance across the two directions are 2.81 Å (green line) and normal to it 2.85 Å (red line) (see Fig. 5e). The region 3 has ridgeline phase of beryllene, in which linear array of atoms separated by bottom lying atoms between them (see Fig. 5e region 3 and below interatomic distances). Interestingly, the interatomic interaction between Be atoms of beryllene and C atoms of CNT changes the

lattice parameters. Raman spectra of Be-CNTs exhibit peaks at 226, 284, 477 and 647 cm^{-1} corresponding to Be and peaks at 1342, 1569 and 2687 cm^{-1} belonging to CNT (see Fig. 5f)[39–41,56]. Raman mapping was carried out to identify differences in hybridized 2D sheets of CNT and beryllene (see Fig. 5g, h). The relative intensity mapping for both materials was carried out at the same location, which confirms the presence of both Be and C (CNT) in the Be-CNT hybrid.

Magnetic behavior of beryllene-based hybrids was also investigated. The saturation magnetization (M_s) obtained at room temperature was 1.91 and 2.08 emu/g at room temperature (300 K) and 60 K, respectively (see Fig. 6a). This observation suggests that strong interlayer S-P_z orbital hybridization at the interface of Be and graphene plays an important role in delivering magnetic nature to Be-G hybrid through s-s coupling. More specifically, an on-site atomic hybridization between the s and p atomic orbitals occurs around the Be nucleus leading to hybrid states with mixed s and p characters. Here, we report the magnetism in s and p block elements. As is evident from FC-ZFC

measurements, T_{C1} and T_{C2} are observed at 290 and 157 K (see Fig. 6b). T_{C1} is the Curie temperature of the samples, and T_{C2} is the critical ordering temperature. Ferromagnetic properties of Be-G hybrids are further imaged by magnetic force microscopy (MFM) measurements at room temperature without any external magnetic field. When the thickness of Be-G sheets was ~115 nm, the shape of magnetic domain walls is a mixture of strips and random magnetic domains (see Fig. 6c along with color intensity

profile depicting the variation in thickness)[46]. The magnetization is high at the interface due to the exchange of spin-polarized electrons. Be-CNT hybrid has been observed in ferromagnetic hysteresis loop not only at 60 K but rather even at room temperature (300 K). The obtained saturation magnetization was 1.84 and 2.65 emu/g at room temperature and 60 K, respectively (see Fig. 6d. The π electron cloud of CNT unveils a strong hybridization with the atomic orbital of beryllene which renders a superior hysteresis loop. The magnetization vs temperature (M-T) measurements reveal the intrinsic details, T_{c1} and T_{c2} are observed at 315 and 198 K, respectively (see Fig. 6e). The enhanced T_{c1} and T_{c2} indicate the strong out-of-plane coupling and minimal defects formation in Be-CNT hybrid. However, the magnetic moments induced by point defects or edges are relatively weak and unstable; and consequently, the ferromagnetic ordering often collapses at low temperatures[57]. The low-temperature ferromagnetic ordering in Be-G and Be-CNT confirms minimal defects density and functionalization. Moreover, in comparison to Be-G, 2D-1D hybrid Be-CNT has fewer defects, which consequently enhances curie temperature. The MFM topographic imaging of Be-CNT hybrids with thickness varying from −9.7 to 10.8 nm is shown in Fig. 6d. The shape of magnetic domain walls is more linear in comparison to the Be-G hybrids. It is evident from the MFM of Be-G and Be-CNT that when the thickness of sheets is lesser, more clear and more precise, the magnetic domain walls are observed. Therefore, the well-arranged magnetic domain walls in Beryllene-based hybrids give the ferromagnetic character. DFT band structure calculations for Be-G hybrids display a very small
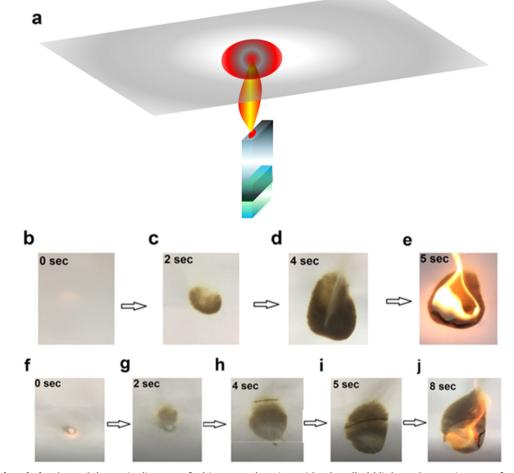

Fig. 7 SERS-based molecular sensing. a–c Schematic diagram of SERS measurements of beryllene employing Be/Au/BSG (borosilicate glass), Au/BSG and BSG as a substrate, respectively. **d** A comparative plot of SERS for methylene blue drop-casted over BSG (borosilicate glass), Au/BSG, and Be/Au/BSG substrates.

Fig. 8 Fire-retardant behavior. a Schematic diagram of white paper burning with a handheld lighter. Camera images of white paper burning with time as it lit fire, **b**–**e** without any coating and **f**–**j** with beryllene coating.

band gap (0.14 eV) opening due to the overlapping of s and p orbitals (see Fig. 6h. The charge density profile displays the interaction between s (of Be) and p_z (of G) orbitals of the Be-G hybrid (see Fig. 6i).

SERS-based molecular sensing

As surface area is high and due to π-π interactions they offer, 2D materials are good anchors for adsorbed molecules. These characteristics of beryllene, along with its metallic nature, would help spread the heat at the interface; beryllene is expected to be a good anchor surface for SERS-based molecular sensing. In addition, beryllene has appreciable thermal stability, which is a surplus. Metallic nature of beryllene can be beneficial in signal detection electrically too. Indeed, when we employed beryllene transferred onto gold-coated glass substrate as SERS platform (see Fig. 7a–c), we observed a significant enhancement in Raman signatures of methylene blue anchored upon it (see Fig. 7d).

In order to exploit real-life engineering applications, the fire-retardant and oxidation-resistant behavior of beryllene were examined.
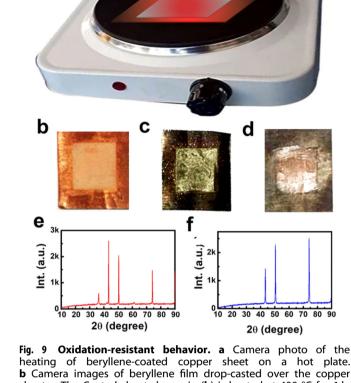
Fire-retardant behavior

We compared the fire resistance behavior of white paper with and without beryllene coating. We observed that where the beryllene coating is there, fire is not spreading in that region when the fire is ignited by a domestic lighter (schematic in Fig. 8a). This depicts the fire-retardant behavior of beryllene (see Fig. 8b–j). The white paper without berylline coating onto it catches fire within 5 s while the paper covered with beryllene takes 8 s to catch fire.

Oxidation-resistant behavior

Anti-oxidation behavior was also invested by studying copper oxidation via hot-plate heating (schematic in Fig. 9a). Copper sheet protected by beryllene sheets coating was heated at 400 °C for 1 h (see Fig. 9b–d). We find that the surface covered by beryllene coating did not oxidize, while the remaining surface was completely oxidized. X-ray diffraction pattern (XRD) of uncovered oxidized region shows new oxide peaks at 36° and 61° along with a change in the intensity ratio of parent metallic peaks (see Fig. 9e, f respectively).

In conclusion, beryllene is a new member of the Xene family that has been discovered and is the lightest known to date. The existence of atomic sheets in sonochemically synthesized samples has been established via a host of microscopic as well as spectroscopic tools and is strongly supported by molecular dynamics simulation results. Two distinct phases, namely square and striped phases, have been observed in HRTEM. Characteristic Raman peaks and XPS measurements confirm the phase purity of Be atomic sheets. Beryllene sheets are experimentally observed to be metallic, and DFT band structure calculation supports this observation. Beryllene hybrids with CNTs and graphene have been synthesized, and their magnetism is explored. SERS-based molecular sensing for methylene blue molecules has been demonstrated by employing beryllene sheets as laminates on gold-coated substrates. Fire-retardant and oxidation-resistant behavior of beryllene have also been explored. While the lightweight of beryllene, along with its electrically conductive nature and optical transparency, invites application as conductive laminates (transparent conducting electrodes and display screens or as conductive nanofillers in polymers keeping its transparency intact), electron-deficient binding in beryllene would be apt for energy generation and storage as well as catalysis. The discovery of this 2D material is expected to lead to new devices, sensors, and phenomena in the coming years.

Fig. 9 Oxidation-resistant behavior. a Camera photo of the heating of beryllene-coated copper sheet on a hot plate. b Camera images of beryllene film drop-casted over the copper sheet. c The Coated sheet shown in (b) is heated at 400 °C for 1 h. d Beryllene itched from a heated copper sheet. e X-ray diffraction (XRD) pattern of image (c). f XRD pattern of image (d).

METHODS

Synthesis of beryllene

For this, 20 mg of beryllium powder (Sigma Aldrich (99.5% purity)) was dispersed in 25 ml of dimethylformamide (DMF) in a quartz vessel (50 ml). The dispersion was then sonicated in a Cole Parmer sonicator (40 kHz) for a time span of 20 h. The supernatant was attained by employing centrifugation. Typically, a Remi R-24 centrifuge machine was used at 5k RPM for 3 min to separate the exfoliated sheets from the remaining part of the sonicated dispersion. The obtained supernatant was dried at 120 °C for 4 h in a nitrogen environment.

Synthesis of beryllene-based hybrids

Firstly, beryllene was synthesized following the same protocol as described above in "Synthesis of beryllene"; however, instead of sonication for 20 h, we sonicate now for 12 h. For Beryllene-graphene hybrid (Be-G), 10 ml solution of beryllene centrifuged at 2k RPM from 12 h sonicated solution was separated, and 5 mg graphene powder was added along with 15 ml DMF making the solution again 25 ml. This resultant solution was again sonicated for 1 h. After sonification, the solution put on a hot plate was dried at 100 °C for 4 h in a nitrogen environment. The dried solution was irradiated microwave in the form of 20 s shots (10 min cooling time between two shots) for a total time of 2 min. The obtained Be-G hybrid was used for characterization. Similarly, following the same protocol and using CNT instead of Graphene, a Beryllene-carbon nanotube (CNT) (Be-CNT) hybrid was synthesized. Beryllene centrifuged 10 ml solution was mixed with 5 mg CNT and 15 ml DMF making 25 ml solvent in the solution. The solution was sonicated for 1 h and dried at 100 °C for 4 h in a nitrogen environment. The dried solution was irradiated microwave in the

form of 20 s shots (10 min cooling time between two shots) for a total time of 2 min. The obtained Be-CNT hybrid was used for characterization.

Characterization techniques

Supernatant of synthesized beryllene was transferred over to a SiO_2 substrate for the study of spectroscopy, microscopy, and other properties. For Raman spectroscopic measurements, a Raman spectrometer having an integrated high-resolution (100X) microscope from Olympus (Seki Techno Tron Corporation, Japan) was used for laser beam focusing as well as to capture the light for micro-optical imaging of beryllene sheets. As an excitation source, a He-Ne laser (wavelength 633 nm) was used in Raman spectroscopy measurements in backscattering geometry. ZEISS Gemini SEM-500 field emission scanning electron microscope (FESEM) was operated in secondary electron detection mode to record the high-resolution images of beryllene. SHIMADZU UV-2600 UV-VIS spectrophotometer was used in the absorption mode for optical transparency. In order to carry out surface-enhanced Raman spectroscopy (SERS), 10 ppm solution of methylene blue (MB) was dropped onto borosilicate glass (BSG), gold-sputtered BSG, and beryllene-coated gold-sputtered BSG for measurements. He-Ne laser (wavelength 633 nm) with a moderate power level (5 mW) was employed in the Raman instrument.

AFM and HRTEM microscopy

An atomic force microscope (AFM) (Agilent, Model No. 5500) in non-contact mode was operated to get a few high-resolution and large-area topographic images of nanometer-thick atomic beryllene sheets using a silicon tip during the measurements. For high-resolution transmission electron microscopy (HRTEM) measurement, beryllene supernatant dispersed in the IPA solvent was spin-coated at 5k RPM (2 min) onto a carbon-coated copper TEM grid (Mesh size = 3 mm) following the standard drying protocol. TEM (JEOL Model No. JEM 2100) was employed in an ultra-high vacuum ($<10^{-6}$ bar) for HRTEM and selected area electron diffraction (SAED) measurements of beryllene sheets.

Photoconductivity measurements

Current vs. Voltage (I-V) and photoconductivity (PC) measurements for beryllene and beryllene-based heterolayers (B/BN and B/MoS$_2$) were done by employing a Keithley source meter (Model No. 2634B) under high vacuum conditions. Two-probe measurements were carried out on beryllene and heterolayers using ultra-fine molybdenum pins. Heterolayers were fabricated onto a SiO_2 substrate, and out-of-plane measurements were done for I-V/PC. For photo-response, optical excitation was carried out using red, green, and blue lasers of wavelengths 650 nm, 532 nm, and 405 nm, respectively.

Magnetic measurements

Vibrating sample magnetometer integrated physical property measurements system (Versa lab, Quantum, Design) has opted for magnetic analyses. Magnetization and magnetic intensity (M-H) hysteresis for 5 mg of synthesized beryllene centrifuged at 6000 RPM was recorded at 300 K and 60 K with magnetic intensity range from −3 to 3 Tesla (T), Also, the temperature variation of magnetization in the temperature range 300 K to 60 K. Additionally, to investigate the phase transition, Zero Field Cooled (ZFC) and Field Cooled (FC) curve were measured, a magnetic field of 1000 Oersted is implemented during FC measurements.

Computational details

We have performed all the Density Functional Theory (DFT) based calculations using the Vienna Ab initio Simulation Package (VASP). We have used the Perdew–Burke–Ernzerhof (PBE) functional within the generalized gradient approximation (GGA)[58]. We have employed Projected augmented-wave (PAW) potential to include the interaction between valence electrons and ion-core[59,60]. A plane-wave basis set with an energy cutoff of 500 eV was used in all the calculations. We have also performed a Born Oppenheimer molecular dynamics (BOMD) simulation to consider the stability of the sheet at room temperature. We have performed a constant-temperature Molecular dynamics (MD simulation considering the NVT canonical ensemble, where we have used a Nose-Hoover thermostat to adjust the temperature at 300 K during the simulations, and we have considered a time step of 0.5 fs[61,62]. We have calculated the trajectory up to 50 ps. The bilayer calculation reveals that the two layers combine together to form a monolayer type of structure, where the charge density contribution comes mainly from the middle layer Be atoms.

DATA AVAILABILITY

The data that support the findings of this study are available from the corresponding authors upon request.

REFERENCES

1. Novoselov, K. S. et al. Electric field effect in atomically thin carbon films. *Science* **306**, 666–669 (2004).
2. Geim, A. K. & Novoselov, K. S. The rise of graphene. *Nat. Mater.* **6**, 183–191 (2007).
3. Marguerite, A. et al. Imaging work and dissipation in the quantum Hall state in graphene. *Nature* **575**, 628–633 (2019).
4. Churchill, H. O. & Jarillo-Herrero, P. Phosphorus joins the family. *Nat. Nanotechnol.* **9**, 330–331 (2014).
5. Qiao, J., Kong, X., Hu, Z. X., Yang, F. & Ji, W. High-mobility transport anisotropy and linear dichroism in few-layer black phosphorus. *Nat. Commun.* **5**, 4475 (2014).
6. Tao, L. et al. Silicene field-effect transistors operating at room temperature. *Nat. Nanotechnol.* **10**, 227–231 (2015).
7. Zhao, J. et al. Rise of silicene: a competitive 2D material. *Prog. Mater. Sci.* **83**, 24–151 (2016).
8. Balendhran, S., Walia, S., Nili, H., Sriram, S. & Bhaskaran, M. Elemental analogues of graphene: silicene, germanene, stanene, and phosphorene. *Small* **11**, 640–652 (2015).
9. Dávila, M. E., Xian, L., Cahangirov, S., Rubio, A. & Le Lay, G. Germanene: a novel two-dimensional germanium allotrope akin to graphene and silicone. *N. J. Phys.* **16**, 095002 (2014).
10. Zhu, F. F. et al. Epitaxial growth of two-dimensional stanene. *Nat. Mater.* **14**, 1020–1025 (2015).
11. Pumera, M. & Sofer, Z. 2D monoelemental arsenene, antimonene, and bismuthene: beyond black phosphorus. *Adv. Mater.* **29**, 1605299 (2017).
12. Yuhara, J., He, B., Matsunami, N., Nakatake, M. & Lay, L. G. Graphene's latest cousin: plumbene epitaxial growth on a 'nano water cube. *Adv. Mater.* **31**, 1901017 (2019).
13. Mannix, A. J., Zhang, Z., Guisinger, N. P., Yakobson, B. I. & Hersam, M. C. Borophene as a prototype for synthetic 2D materials development. *Nat. Nanotechnol.* **13**, 444–450 (2018).
14. Ranjan, P. et al. Freestanding borophene and its hybrids. *Adv. Mater.* **31**, 1900353 (2019).
15. Ranjan, P., Lee, J. M., Kumar, P. & Vinu, A. Borophene: new sensation in flatland. *Adv. Mater.* **32**, 2000531 (2020).
16. Chahal, S. et al. Borophene via micromechanical exfoliation. *Adv. Mater.* **33**, 2102039 (2021).
17. Chahal, S., Bandyopadhyay, A., Dash, S. P. & Kumar, P. Microwave synthesized 2D gold and its 2D-2D hybrids. *J. Phys. Chem. Lett.* **13**, 6487–6495 (2022).
18. Coroş, M., Pogăcean, F., Măgeruşan, L., Socaci, C. & Pruneanu, S. A brief overview on synthesis and applications of graphene and graphene-based nanomaterials. *Front. Mater. Sci.* **13**, 23–32 (2019).
19. Torrisi, S. B., Singh, A. K., Montoya, J. H., Biswas, T. & Persson, K. A. Two-dimensional forms of robust CO_2 reduction photocatalysts. *NPJ 2D Mater. Appl.* **4**, 24 (2020).
20. Wang, Z. Q., Lü, T. Y., Wang, H. Q., Feng, Y. P. & Zheng, J. C. Review of borophene and its potential applications. *Front. Phys.* **14**, 33403 (2019).

21. Kou, L., Chen, C. & Smith, S. C. Phosphorene: fabrication, properties, and applications. *Phys. Chem. Lett.* **6**, 2794–2805 (2015).

22. Chahal, S., Kauzlarich, S. M. & Kumar, P. Microwave synthesis of hematene and other 2D oxides. *ACS Mater. Lett.* **3**, 631–640 (2021).

23. Chahal, S. et al. Microwave flash synthesis of phosphorus and sulphur ultradoped graphene. *Chem. Eng. J.* **450**, 138447 (2022).

24. Chahal, S. et al. Transition metal-doped boron nitride atomic sheets with an engineered bandgap and magnetization. *J. Phys. Chem. C* **126**, 21084–21093 (2022).

25. Vishwakarma, K. et al. Quantum-coupled borophene-based heterolayers for excitonic and molecular sensing applications. *Phys. Chem. Chem. Phys.* **24**, 12816–12826 (2022).

26. Cao, Y. et al. Unconventional superconductivity in magic-angle graphene superlattices. *Nature* **556**, 43–50 (2018).

27. Lee, S., Kumar, P., Hu, Y., Cheng, G. J. & Irudayaraj, J. Graphene laminated gold bipyramids as sensitive detection platforms for antibiotic molecules. *Chem. Commun.* **51**, 15494–15497 (2015).

28. Hu, Y. et al. Water flattens graphene wrinkles: laser shock wrapping of graphene onto substrate-supported crystalline plasmonic nanoparticle arrays. *Nanoscale* **7**, 19885–19893 (2015).

29. Hu, Y. et al. Controlled and stabilized light–matter interaction in graphene: plasmonic film with large-scale 10-nm lithography. *Adv. Opt. Mater.* **4**, 1811–1823 (2016).

30. Das, S. R. et al. Single-layer graphene as a barrier layer for intense UV laser-induced damages for silver nanowire network. *ACS Nano* **9**, 11121–11133 (2015).

31. Qurashi, A., Subrahmanyam, K. S. & Kumar, P. Nanofiller graphene–ZnO hybrid nanoarchitecture: optical, electrical and optoelectronic investigation. *J. Mater. Chem. C* **3**, 11959–11964 (2015).

32. Liu, J., Kumar, P., Hu, Y., Cheng, G. J. & Irudayaraj, J. M. K. Enhanced multiphoton emission from CdTe/ZnS quantum dots decorated on single-layer graphene. *J. Phys. Chem. C* **119**, 6331–6336 (2015).

33. Park, H., Brown, P. R., Bulović, V. & Kong, J. Graphene as transparent conducting electrodes in organic photovoltaics: studies in graphene morphology, hole transporting layers, and counter electrodes. *Nano Lett.* **12**, 133–140 (2012).

34. Beiss, P., Ruthardt, R. & Warlimont, H. Materials powder metallurgy data. Refractory, hard and intermetallic materials. *Landolt-Börnstein-Group VIII Adv. Mater. Technol.* **2**, 59–89 (2002).

35. Gonçalves, P. A. D., Xiao, S., Peres, N. M. R. & Mortensen, N. A. Hybridized plasmons in 2D nanoslits: from graphene to anisotropic 2D materials. *ACS Photonics* **4**, 3045–3054 (2017).

36. Mittendorff, M., Li, S. & Murphy, T. E. Graphene-based waveguide-integrated terahertz modulator. *ACS Photonics* **4**, 316–321 (2017).

37. Fan, Y., Zhao, M., Wang, Z., Zhang, X. & Zhang, H. Tunable electronic structures of graphene/boron nitride heterobilayers. *Appl. Phys. Lett.* **98**, 083103 (2011).

38. Sergeeva, A. P. et al. Understanding boron through size-selected clusters: structure, chemical bonding, and fluxionality. *Acc. Chem. Res.* **47**, 1349 (2014).

39. Yoon, S. et al. Crystalline beryllium oxide on Si (100) deposited using E-beam evaporator and thermal oxidation. *Appl. Surf. Sci.* **479**, 803–809 (2019).

40. Kumar, M. et al. JET contributors. Identification of BeO and BeOxDy in melted zones of the JET Be limiter tiles: Raman study using comparison with laboratory samples. *Nucl. Mater. Energy* **17**, 295–301 (2018).

41. Rusu, M. I. et al. Preparing the future post-mortem analysis of beryllium-based JET and ITER samples by multi-wavelengths Raman spectroscopy on implanted Be, and co-deposited Be. *Nucl. Fusion* **57**, 076035 (2017).

42. Mallinson, C. F., Castle, J. E. & Watts, J. F. Beryllium and beryllium oxide by XPS. *Surf. Sci. Spectra* **20**, 86 (2013).

43. Mallinson, C. F., Castle, J. E. & Watts, J. F. Analysis of the Be KLL auger transition on beryllium and beryllium oxide by AES. *Surf. Sci. Spectra* **20**, 97 (2013).

44. Simos, N., Elbakhshwan, M., Zhong, Z., Ghose, S. & Savkliyildiz, I. High-temperature annealing of proton irradiated beryllium e A dilatometry-based study. *J. Nucl. Mater.* **477**, 1–17 (2016).

45. Zheng, H. et al. Grain boundary properties of elemental metals. *Acta Mater.* **186**, 40–49 (2020).

46. Wu, H. et al. Strong intrinsic room-temperature ferromagnetism in freestanding non-van der Waals ultrathin 2D crystals. *Nat. Commun.* **12**, 5688 (2021).

47. Li, J. I. A. et al. Pairing states of composite fermions in double-layer graphene. *Nat. Phys.* **15**, 898–903 (2019).

48. Koshino, M. Interlayer interaction in general incommensurable atomic layers. *N. J. Phys.* **17**, 015014 (2015).

49. Shi, Y. et al. Self-assembly of hierarchical MoS_x/CNT nanocomposites (2<x<3): towards high performance anode materials for lithium ion batteries. *Sci. Rep.* **3**, 2169 (2013).

50. Bindumadhavan, K., Srivastava, S. K. & Mahanty, S. MoS_2–MWCNT hybrids as a superior anode in lithium-ion batteries. *Chem. Commun.* **49**, 1823–1825 (2013).

51. Ma, H., Du, S., Tao, H., Li, T. & Zhang, Y. Three-dimensionally integrated carbon tubes/MoS_2 with reduced graphene oxide foam as a binder-free anode for lithium ion battery. *J. Electroanal. Chem.* **823**, 307–314 (2018).

52. Das, S., Dutta, A., Bera, R. & Patra, A. Ultrafast carrier dynamics in 2D–2D hybrid structures of functionalized GO and CdSe nanoplatelets. *Phys. Chem. Chem. Phys.* **21**, 15568–15575 (2019).

53. Chen, J., Xu, X., Li, T., Pandiselvi, K. & Wang, J. Toward high performance 2D/2D hybrid photocatalyst by electrostatic assembly of rationally modified carbon nitride on reduced graphene oxide. *Sci. Rep.* **6**, 37318 (2016).

54. O'Brien, M. et al. Mapping of low-frequency Raman modes in CVD-grown transition metal dichalcogenides: layer number, stacking orientation and resonant effects. *Sci. Rep.* **6**, 19476 (2016).

55. Malard, L. M., Pimenta, M. A., Dresselhaus, G. & Dresselhaus, M. S. Raman spectroscopy of graphene. *Phys. Rep.* **473**, 51–87 (2009).

56. Dresselhaus, M. S., Dresslhaus, G., Saito, R. & Jorio, A. Raman spectroscopy of carbon nanotubes. *Phys. Rep.* **409**, 47–99 (2005).

57. Hu, W. et al. Embedding atomic cobalt into graphene lattices to activate room-temperature ferromagnetism. *Nat. Commun.* **12**, 1854 (2021).

58. Perdew, J. P., Burke, K. & Ernzerhof, M. Generalized gradient approximation made simple. *Phys. Rev. Lett.* **77**, 3865 (1996).

59. Mortensen, J. J., Hansen, L. B. & Jacobsen, K. W. Real-space grid implementation of the projector augmented wave method. *Phys. Rev. B* **71**, 035109 (2005).

60. Kresse, G. & Joubert, D. From ultrasoft pseudopotentials to the projector augmented-wave method. *Phys. Rev. B Condens. Matter Mater. Phys.* **59**, 1758 (1999).

61. Nosé, S. A unified formulation of the constant temperature molecular dynamics methods. *J. Chem. Phys.* **81**, 511 (1984).

62. Hoover, W. G. Canonical dynamics: equilibrium phase-space distributions. *Phys. Rev. A* **31**, 1695 (1985).

ACKNOWLEDGEMENTS

AUTHOR CONTRIBUTIONS

P.K. conceived the idea. S.C. carried out all the experimental work, including synthesis, characterization, and applications of beryllene. A.B. carried out theoretical calculations. The electrical and excitonic behavior of beryllene was discussed with C.S.Y. S.C., C.S.Y. and P.K. wrote the manuscript together. The whole project was carried out under the overall supervision of PK.

COMPETING INTERESTS

The authors declare no competing interests.

ETHICS

The research did not involve animals, human trials, or hazardous/toxic/banned materials. All the norms set by *Nature* Publication were followed in research and research reporting.

ADDITIONAL INFORMATION

Supplementary information The online version contains supplementary material available at https://doi.org/10.1038/s41699-023-00415-y.

Correspondence and requests for materials should be addressed to Chan-Shan Yang or Prashant Kumar.

Reprints and permission information is available at http://www.nature.com/reprints